



# Metabolic coordination and phase transitions in spatially distributed multi-cellular systems



Krishnadev Narayananakutty <sup>1,2</sup>, José Antonio Pereiro-Morejon <sup>3,4</sup>, Arián Ferrero-Fernández <sup>1,2</sup>, Valentina Onesto <sup>5</sup>, Stefania Forciniti <sup>5</sup>, Loretta L. del Mercato <sup>5</sup>, Roberto Mulet <sup>6</sup>, Andrea De Martino <sup>7,8</sup> , David S. Tourigny <sup>9</sup> & Daniele De Martino <sup>1,10</sup>

During overflow metabolism, cells excrete glycolytic byproducts when growing under aerobic conditions in a seemingly wasteful fashion. While potentially advantageous for microbes with finite oxidative capacity, its role in higher organisms is harder to assess. Recent single-cell experiments suggest overflow metabolism arises due to imbalances in inter-cellular exchange networks. We quantitatively characterize this scenario by integrating spatial metabolic modeling with tools from statistical physics and experimental single-cell flux data. Our results provide a theoretical demonstration of how diffusion-limited exchanges shape the space of accessible multi-cellular metabolic states. Specifically, a phase transition from a balanced network of exchanges to an unbalanced, overflow regime occurs as mean glucose and oxygen uptake rates vary. Heterogeneous single-cell metabolic phenotypes occur near this transition. Time-resolved tumor-stroma co-culture data support the idea that overflow metabolism stems from failure of inter-cellular metabolic coordination. In summary, environmental control is an emergent multi-cellular property, rather than a cell-autonomous effect.

Cell populations adapt to an environment on at least two different levels: (i) via intra-cellular regulation (e.g. metabolic, signaling, genetic), which underlies essential maintenance, biosynthetic and, possibly, replicative processes; and (ii) via extra-cellular mechanisms (e.g. sensing, signaling, motility), necessary to harvest information and control exchanges with the medium. The latter level prompts inter-cellular interactions and introduces an ecological dimension to multi-cellular systems, where cells can be seen as agents that need to meet certain requirements while jointly modulating a shared environment. The way in which the two layers integrate is a key determinant of adaptation, viability, and ultimately fitness<sup>1–4</sup>. This raises a rather basic question: is a viable environment the result of the straightforward aggregation of a large number of autonomous actions by individual cells, or is it rather an emergent property of the collective behavior of many interacting cells? In the former case, intra-cellular constraints (and possibly cell-specific objective functions) effectively direct population behavior<sup>5</sup>.

In the latter, inter-cellular interactions play the central role<sup>6</sup>. Can one quantitatively separate the two contributions?

The contours of this problem become especially clear upon focusing on a cellular process that directly links the two levels described above, namely carbon overflow (CO). In short, CO consists of the excretion into the medium of carbon-based waste products of intra-cellular carbon catabolism, such as acetate, ethanol, or lactate, in aerobic conditions<sup>7,8</sup>. This may occur for instance because the cell's oxidative capacity is saturated (e.g. due to excess glucose availability or dysregulated import pathways), so that, even in the presence of abundant oxygen, incoming carbon is diverted towards fermentation<sup>5,9–11</sup>. CO appears to be a 'universal' feature of cellular metabolism, which has been consistently observed across domains. While in microbial systems it can be partly explained by the evolutionary advantage of a higher growth rate at the cost of lower energy yield<sup>12–15</sup>, the root cause of CO in higher organisms or in tumors (where it underlies the Warburg

<sup>1</sup>Biofisika Institute (CSIC, UPV/EHU), Leioa, Bizkaia, Spain. <sup>2</sup>Department of Molecular Biology and Biochemistry, University of the Basque Country, Leioa, Bizkaia, Spain. <sup>3</sup>Group of Complex Systems and Statistical Physics, Physics Faculty, University of Havana, La Habana, La Habana, Cuba. <sup>4</sup>Biology Faculty, University of Havana, La Habana, La Habana, Cuba. <sup>5</sup>Institute of Nanotechnology, National Research Council (CNR-NANOTEC), Lecce, Puglia, Italy. <sup>6</sup>Department of Theoretical Physics, University of Havana, La Habana, La Habana, Cuba. <sup>7</sup>Politechnico di Torino, Torino, Italy. <sup>8</sup>Italian Institute for Genomic Medicine, c/o IRCCS, Candiolo, Italy. <sup>9</sup>School of Mathematics, University of Birmingham, Birmingham, UK. <sup>10</sup>Ikerbasque – Basque Foundation for Science, Bilbao, Bizkaia, Spain.

e-mail: [andrea.demartino@polito.it](mailto:andrea.demartino@polito.it); [d.tourigny@bham.ac.uk](mailto:d.tourigny@bham.ac.uk); [daniele.demartino@ehu.eus](mailto:daniele.demartino@ehu.eus)

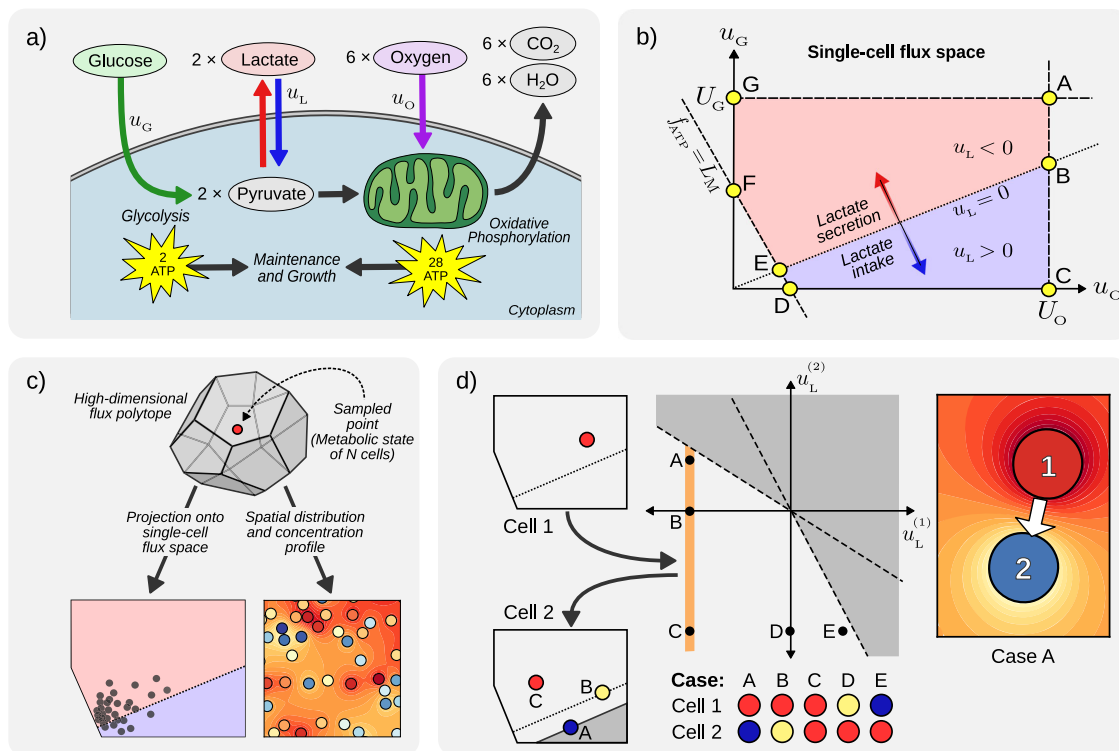


**Fig. 1 | Constraint-based metabolic model.** **a** Sketch of the single-cell metabolic network representing the central carbon pathways ( $u_G$  glucose uptake,  $u_L$  lactate flux,  $u_O$  oxygen uptake). **b** Feasible single-cell flux space ( $\mathcal{F}_1$ ) in the  $(u_O, u_G)$  plane, bounded by Eqs (3) (glucose intake), (4) (oxygen intake), and (5) (ATP maintenance). For a single cell (as well as for the average bulk behavior) the purple region ( $u_L > 0$  or lactate import) is unfeasible unless lactate is exogenously provided. Points A-G are those where the cell would maximize rate of ATP production (A), maximize rate of ATP production with zero net lactate exchange (B), maximize rate of ATP production while using lactate as the only carbon source (C), minimize rate of ATP production while using lactate as the only carbon source (D), minimize rate of ATP

production with zero net lactate exchange (E), minimize rate of ATP production anaerobically (F), or maximize rate of lactate excretion (G). **c** The possibility for cells to exchange lactate defines an extended metabolic flux space for a system of  $N$  cells ( $\mathcal{F}_N$ ) whose configurations can be projected into single-cell flux space. In turn, the corresponding lactate fluxes define a spatial concentration gradient in the medium via (8). **d** Case  $N = 2$ , feasible space in the plane  $(u_L^{(1)}, u_L^{(2)})$ . In cases A and E cells are coupled via lactate exchange, one cell acting as a donor (red) for the other (blue). This makes the  $u_L > 0$  (purple) region of panel (b) viable for the acceptor cell even in absence of an external lactate source.

effect<sup>16</sup>) is more difficult to ascribe, especially when it is not associated with growth and replication<sup>4,17–21</sup>.

An ecological role for CO derives from the fact that accumulation of fermentation byproducts in the extra-cellular medium leads to acidification and, in turn, detrimental effects ranging from the slowdown of protein synthesis to growth inhibition due to apoptosis<sup>22</sup>. Remediation of the shared environment is therefore of paramount importance for cell populations. On the other hand, exporters of overflow products effectively supply the medium with additional carbon equivalents on which cells can rely for sustenance (via oxidation)<sup>23,24</sup>. Importers thereby contribute to correcting environmental pollution. Taken together, these processes are major drivers of functionally- and ecologically-significant inter-cellular crosstalk<sup>25–28</sup>. Nevertheless, how decisive such a crosstalk is compared to individual cellular decisions in engineering the environment remains an open question.

We attempt to address this issue by integrating (a) constraint-based metabolic modeling (CBM)<sup>29</sup> and diffusion constraints, (b) the statistical physics approach to the study of emergent phenomena<sup>30</sup>, and (c) high-resolution data for single-cell behavior in a cell population adapting to a glucose-based medium<sup>31</sup>. More specifically, we first employ CBM to demonstrate that a spatially distributed population of cells with identical metabolic requirements coupled through an exchange network undergoes a crossover between two distinct metabolic regimes when the population-averaged metabolic rate changes. The first regime is characterized by weak medium acidification, while significant accumulation of overflow products occurs in the second. Next, we rationalize these findings mathematically using a highly stylized but analytically tractable version of the model. Within this approach, the crossover takes the form of an order-disorder transition

similar to those that characterize thermodynamic systems in statistical physics<sup>30</sup>, and bulk overflow appears as an emergent feature of a population of interacting cells. Finally, building on the theory, we exploit statistical inference techniques to reconstruct the metabolic trajectory of an experimentally-studied mixed population of cancer cells and cancer-associated fibroblasts that displays the Warburg effect and self-organizes its collective metabolism over time to reduce lactate spillover via metabolic exchanges. We will focus on the lag phase with negligible glucose depletion and growth, because it provides insights into the cellular and molecular mechanisms that govern cancer cell adaptation and subsequent proliferation. We show in particular that the population, while coordinating at the metabolic level and reducing lactate spillover, collectively moves towards states where the ATP yield on glucose is optimal. This provides a quantitative, low-dimensional, and interpretable representation of the complex, high-dimensional dynamics of the population in the space of feasible metabolic states.

## Results

### Single-cell metabolic model and flux space

To build our theoretical setup, we begin by modeling the metabolic flux space available to a single mammalian cell through CBM with the minimal reaction network for energy production by central carbon pathways displayed in Fig. 1a. This simplistic model consists of just three metabolic reactions that carry out (a) the import and conversion of glucose to pyruvate (representing glycolysis), (b) the interconversion of pyruvate and lactate (representing lactate import/export), and (c) the generation of ATP using pyruvate and oxygen (representing oxidative phosphorylation). We want to

model a typical overflow scenario like the one presented in<sup>31</sup>, where the medium is glucose enriched, there is lactate accumulation in aerobic conditions and metabolism is running mainly for the sake of energy production with negligible biomass build-up. This corresponds to the initial part of the growth curve, during which the population adapts to the environment.

Because the experimental timescales we consider (hours after seeding) are much longer than typical metabolite turnover times (seconds for ATP)<sup>32–34</sup>, we can make the same stationarity assumption for metabolite levels that is standard in approaches based on Flux Balance Analysis<sup>35</sup>. At steady state, the equation for carbon mass-balance is

$$u_G + \frac{u_L}{2} - \frac{u_O}{6} = 0, \quad (1)$$

where  $u_G \geq 0$  is the flux for import of glucose from the environment (in units mmol/gh),  $u_L$  is the corresponding lactate exchange flux ( $u_L > 0$  for import,  $u_L < 0$  for export) and  $u_O \geq 0$  is the flux for import of molecular oxygen (that we assume corresponds to respiratory flux, so that it enters the carbon mass-balance due to its equivalence to carbon dioxide secretion). The net rate of ATP production is instead given by

$$f_{\text{ATP}} = -u_L + 5u_O, \quad (2)$$

where we used empirical coefficients for ATP produced by respiration and fermentation pathways (Supplementary Note 1). Along with (1), the space of viable fluxes is defined by the additional constraints

$$0 \leq u_G \leq U_G \quad (3)$$

$$0 \leq u_O \leq U_O \quad (4)$$

$$f_{\text{ATP}} \geq L_M \quad (5)$$

representing respectively the limited capacities of glucose import channels (Eq. (3)) and mitochondrial activity (Eq. (4)), and a minimal rate of energy production required for cell maintenance (Eq. (5)). Values for the parameters  $U_G$ ,  $U_O$  and  $L_M$  are also available from the literature (Supplementary Note 1).

The resulting single-cell flux space is represented by the 2-dimensional polytope in the  $(u_O, u_G)$  plane shown in Fig. 1b, whose oblique boundary corresponds to the maintenance requirement (5). Lactate fluxes can be read off from (1). The line separating the purple and pink shaded regions corresponds to states with  $u_L = 0$ . States with constant but non-zero lactate exchange are represented by lines parallel to it. In particular, states with  $u_L > 0$  (resp.  $u_L < 0$ ), i.e. with lactate import (resp. export) foliate the purple (resp. pink) shaded region. In the absence of environmental lactate, an isolated cell can only attain states with  $u_L \leq 0$  (lactate import is not allowed). In the presence of a lactate source, however, states with  $u_L > 0$  become accessible (lactate import is allowed). We shall use the symbol  $\mathcal{F}_1$  to denote the viable single-cell flux space of Fig. 1b. An independent cell that autonomously adjusts its metabolism to optimize a linear objective function (as in Flux Balance Analysis<sup>35</sup>) would be found at specific points on the boundary of  $\mathcal{F}_1$ . For instance (Fig. 1b), at point A it maximizes the rate of ATP production. (More examples are given in the caption of Fig. 1).

### Exchange coupling and multi-cellular flux space

When  $N$  cells share the same extra-cellular environment, lactate-excreting cells effectively act as lactate sources. This makes the  $u_L > 0$  portion of  $\mathcal{F}_1$  (purple region in Fig. 1b) potentially accessible to other cells even if there is no external source of lactate in the culture. Cells therefore become metabolically coupled through the exchange of lactate, as endogenous lactate is shuttled across the population by diffusion. By modeling cells as spherical sources or sinks of lactate, with radius  $R$  and located at fixed positions  $\mathbf{r}_i$  ( $i = 1, 2, \dots, N$ ), one can show that, at steady state (i.e. in practice for

timescales larger than the diffusion time of lactate across the experimental length-scale we consider, which roughly equals  $L^2/D_L \simeq 4$  min, with  $L = 0.5$  mm the system size and  $D_L \simeq 700 \mu\text{m}^2/\text{s}$  the diffusion constant of lactate), the lactate exchange fluxes  $u_L^{(i)}$  of all cells must obey an additional set of  $N$  constraints described by (Supplementary Note 2; see also<sup>36</sup>)

$$\sum_{j=1}^N A_{ij} u_L^{(j)} \leq 0 \quad (i = 1, 2, \dots, N), \quad (6)$$

$$A_{ij} = \delta_{ij} + (1 - \delta_{ij}) \frac{R}{|\mathbf{r}_i - \mathbf{r}_j|} > 0, \quad (7)$$

where  $|\mathbf{r}_i - \mathbf{r}_j| \geq 2R$  and  $\delta_{ij} = 1$  if  $i = j$  and zero otherwise. In rough words, these constraints effectively couple cells by imposing that the net consumption of lactate across the culture can not exceed its endogenous supply. However, the generalization that accounts for an exogenous lactate source or for lactate accumulated in the culture is straightforward (Supplementary Method 4). In principle, similar diffusional coupling constraints hold for glucose and oxygen. For the cell densities we consider, though, they are immaterial (i.e. cells do not compete for either of the two, see Supplementary Method 5). Combined with  $N$  copies of (1) and (3)–(5), one for each cell  $i$ , the inequalities (6) define a  $2N$ -dimensional convex polytope containing the feasible flux configurations of a system of  $N$  cells coupled through diffusion-limited lactate exchanges (Fig. 1c). We henceforth denote this space by  $\mathcal{F}_N$ . In turn, each point in  $\mathcal{F}_N$  can be represented by  $N$  points in the single-cell space  $\mathcal{F}_1$  (one per cell, Fig. 1c). Finally, it is possible to reconstruct the spatial concentration profile of lactate by assuming that lactate levels in the culture obey the Laplace equation. Specifically, the concentration at position  $\mathbf{r}$  is given by (Supplementary Note 2)

$$c_L(\mathbf{r}) = \sum_{i=1}^N \frac{u_L^{(i)}}{D_L |\mathbf{r} - \mathbf{r}_i|} + B(\mathbf{r}), \quad (8)$$

where  $B(\mathbf{r})$  is a term accounting for exchanges with the boundary of the system. (Note that we are assuming that cells are identical, in that the parameters  $U_G$ ,  $U_O$ ,  $L_M$  and  $R$  are the same for each cell.)

The effect of the diffusion constraint is most easily visualized diagrammatically in the case of two cells ( $N = 2$ , Fig. 1d), where the maximal lactate uptake rate for one cell is determined by both a minimum rate of lactate production by the other and the distance between them (reflected in the slopes of the dashed lines in Fig. 1d). Clearly, (6) does not allow for both cells to import lactate ( $u_L^{(1)} > 0$ ,  $u_L^{(2)} > 0$ ) if none is supplied externally. This picture generalizes to  $N$  cells: it can be shown (Supplementary Note 3) that environmental lactate accumulation ( $\sum_{i=1}^N u_L^{(i)}$ ) can not be zero unless the lactate flux of each individual cell vanishes. Conversely, if lactate is exchanged between any cells within the population then there must be some non-zero leakage of lactate in the medium, i.e. an accumulation of overflow product akin to the Warburg effect.

### Environmental lactate spillover as a failure of inter-cellular coordination

While constraints (1) and (3)–(6) define the space  $\mathcal{F}_N$  of feasible multi-cellular metabolic flux configurations and implicitly include a lactate exchange network, interpreting  $\mathcal{F}_N$  in terms of population-level metabolic states is not straightforward. To gain a deeper understanding, we resorted to a statistical approach based on sampling  $\mathcal{F}_N$  according to a controllable probabilistic rule. A simple and theoretically convenient choice for a probability density over the  $2N$ -dimensional flux space is given by the Boltzmann distribution<sup>37</sup>

$$p(\underline{\mathbf{u}}|\beta) = \frac{\exp[\beta h(\underline{\mathbf{u}})]}{Z(\beta)} \quad (\underline{\mathbf{u}} \in \mathcal{F}_N), \quad (9)$$

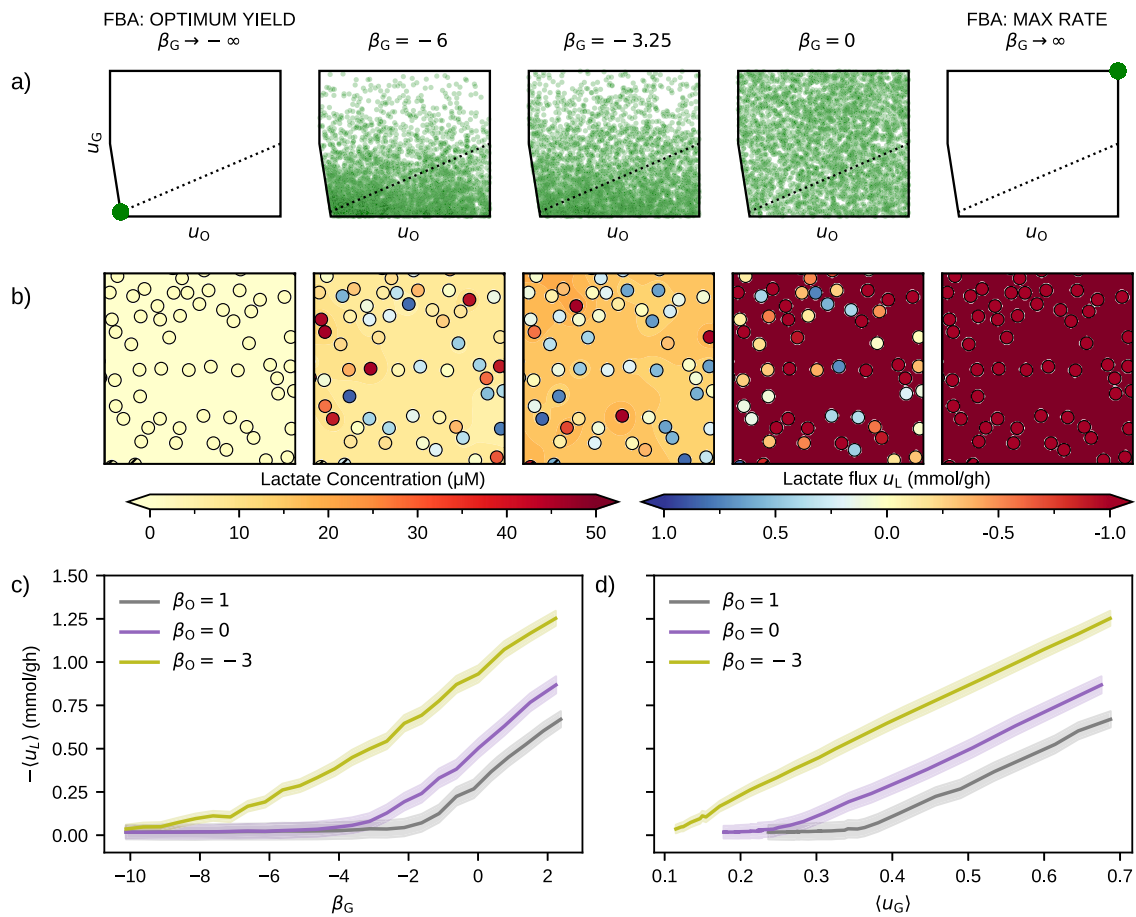


**Fig. 2 | Emergent bulk overflow in CBM simulations.** Simulations are performed by sampling the feasible space  $\mathcal{F}_N$  for  $N = 150$  cells distributed over an area of  $500 \times 500 \mu\text{m}^2$  according to (13) via Hit-and-Run Monte Carlo Markov chains for fixed  $\beta_O = 0$  and different values of  $\beta_G$ . This interpolates between the states of maximum ATP yield ( $\beta_G \rightarrow -\infty$ ) and maximum ATP rate ( $\beta_G \rightarrow \infty$ ). **a** Multi-cellular flux configurations projected into single-cell space in the  $(u_O, u_G)$  plane

(same as in Fig. 1b) for different values of  $\beta_G$ . **b** Typical spatial lactate concentration gradient across the culture (background color) and single cell lactate fluxes (colored circles) for the same values of  $\beta_G$  as in (a). **c** Mean net lactate excretion fluxes  $(-\langle u_L \rangle)$  as a function of  $\beta_G$  and (d) of the mean glucose uptake for different values of  $\beta_O$ . The shaded region indicates standard error on the mean. Notice the approximately threshold-linear behavior for larger values of  $\beta_O$ .

where  $\underline{u} \equiv \{(u_G^{(i)}, u_O^{(i)})\}_{i=1}^N$  denotes an  $N$ -cell configuration of metabolic degrees of freedom,  $\beta$  is a numerical parameter,  $h$  is a prescribed function of the glucose and oxygen import fluxes of every cell, while

$$Z(\beta) = \int_{\mathcal{F}_N} \exp[\beta h(\underline{u})] d\underline{u} \quad (10)$$

is a factor ensuring normalization over  $\mathcal{F}_N$ . For  $\beta = 0$ , (9) coincides with the uniform distribution over  $\mathcal{F}_N$ , under which each viable  $N$ -cell state is equally likely. When  $\beta \rightarrow +\infty$  (resp.  $\beta \rightarrow -\infty$ ), instead, the sampling concentrates on  $N$ -cell states of maximum (resp. minimum)  $h$ . Notably, since

$$\langle h \rangle_\beta \equiv \frac{1}{N} \int_{\mathcal{F}_N} h(\underline{u}) p(\underline{u}|\beta) d\underline{u} = \frac{\partial}{\partial \beta} \ln Z(\beta), \quad (11)$$

$$\sigma_h^2 \equiv \langle h^2 \rangle_\beta - \langle h \rangle_\beta^2 = \frac{\partial^2}{\partial \beta^2} \ln Z(\beta), \quad (12)$$

fixing the value of  $\beta$  is equivalent to constraining the population-averaged value of  $h$  while still allowing for variability in single-cell metabolic profiles. Most importantly, for any  $\beta$ , (9) describes the distribution with constrained mean value of  $h$  having *maximum entropy* and, therefore, minimum extra bias<sup>37</sup>. As  $\beta$  changes, therefore, (9) allows for the exploration of a broad range of population-level features.

Previous applications of maximum-entropy frameworks to metabolic data mainly focused on bacterial growth, where the biomass synthesis rate is a natural choice for  $h$ <sup>38,39</sup>. Here we want to focus instead on the adaptation part of the dynamics, during which biomass synthesis is negligible<sup>31</sup>. In this regime, natural choices for  $h$  are the overall glucose and oxygen import fluxes, as they represent the key independent degrees of freedom the culture can coordinate to control. Any other linear function (e.g., ATP production) can be obtained from these via linear combination. We therefore opted for a version of (9) that allows to maximize or minimize these quantities independently, i.e. ( $\underline{u} \in \mathcal{F}_N$ )

$$p(\underline{u}|\beta_G, \beta_O) \propto \exp \left[ \beta_G \sum_{i=1}^N u_G^{(i)} + \beta_O \sum_{i=1}^N u_O^{(i)} \right], \quad (13)$$

where  $\beta_G$  and  $\beta_O$  are real parameters, and sampled the space  $\mathcal{F}_N$  according to (13) for different values of  $\beta_G$  and  $\beta_O$  via Hit-and-Run Monte Carlo (Supplementary Method 2, and ref. 39). (Identities similar to (11) and (12) valid for (13) are given in Supplementary Method 1). Representative configurations for 150 cells uniformly scattered at random over an area of  $0.5 \times 0.5 \text{ mm}^2$  are showcased in Fig. 2a.

We focus on the case where  $\beta_O$  is fixed to a finite value and  $\beta_G$  is varied from  $-\infty$  to  $+\infty$  (Fig. 2a, b), thereby modulating the mean glucose consumption in the population from minimal to maximal. When  $\beta_G \rightarrow -\infty$ , cells independently maximize their ATP/glucose yields (Fig. 2a, leftmost

panel), corresponding to point E in Fig. 1b. With our (biologically plausible) choice of parameters, this leads to a homogeneous configuration where all cells run on respiration, none produce lactate, and thus no lactate accumulates in the medium (Fig. 2b, leftmost panel). As  $\beta_G$  increases, cells begin to excrete and import lactate, leading to highly heterogeneous lactate fluxes. Remarkably, the resulting spillover is very small, implying that the lactate exchange network is nearly balanced in spite of the presence of large excretion fluxes. However, a further increase in  $\beta_G$  destabilizes the network, causing lactate to accumulate in the medium at significant levels (Fig. 2a, b, middle panels). Finally, for  $\beta_G \rightarrow +\infty$ , when cells independently maximize their ATP production rates (Fig. 2a, rightmost panel), the population returns to a homogeneous state in which all cells run strongly on fermentation and excrete large amounts of lactate (Fig. 2b, rightmost panel). This corresponds to point A in Fig. 1b.

The crossover from the state of maximum ATP yield to the state of maximum ATP rate is clearly reflected by the fact that the average net flux of lactate excretion across the population ( $-\langle u_L \rangle$ ) increases as  $\beta_G$  increases (Fig. 2c). We observe that a range of values of  $\beta_O$  exists for which  $-\langle u_L \rangle$  closely resembles a threshold-linear function of  $\beta_G$ , marking a sharp transition between regimes with small and large lactate spillover, respectively. Such a behavior is reminiscent of that of an order parameter in standard order-disorder transitions in statistical physics (e.g., see ref. 40, Ch. 3).

To summarize, numerical exploration of the feasible space of a multi-cellular metabolic system subject to diffusion-limited lactate exchange suggests that the metabolic activity of cells gives rise to a complex and highly heterogeneous interaction network that couples lactate producers to lactate importers. Environmental lactate accumulation may emerge from imbalances in this network that, depending on the mean oxygen consumption ( $\beta_O$ ), can set in abruptly as  $\beta_G$  (i.e. the average net glucose consumption rate) increases. Finally, the model is able to reproduce in a stylized way typical bulk overflow-rate curves<sup>8,12,41</sup>, unraveling the underlying single-cell dynamics.

### Mean-field theory links the emergent threshold behavior to a phase transition

To elucidate the behavior uncovered by sampling  $\mathcal{F}_N$  for varying  $\beta_G$  and  $\beta_O$ , we analyzed a mathematically solvable approximation of our constraint-based model. To define it, we focused in particular on the set of constraints (6), which distinguishes  $\mathcal{F}_N$  from  $N$  independent copies of the single-cell space  $\mathcal{F}_1$ . Upon isolating the contribution of cell  $i$ , the diffusion constraints (6) can be re-cast as

$$u_L^{(i)} + \sum_{j \neq i} A_{ij} u_L^{(j)} \leq 0 \quad (i = 1, 2, \dots, N). \quad (14)$$

The sum on the left-hand-side depends on the specific values of the fluxes  $u_L^{(j)}$  as well as on the relative positions of cells (see (7)). For the sake of tractability, we however assume  $N \gg 1$  and replace all coefficients  $A_{ij}$  with an  $N$ -dependent constant factor  $K/N$ , thereby discarding effects due to the spatial organization of cells so that all pairs of cells interact with the same strength. To estimate  $K$ , we note that, upon neglecting fluctuations,

$$\sum_{j \neq i} A_{ij} u_L^{(j)} \simeq K \bar{u}_L, \quad (15)$$

where  $\bar{u}_L$  denotes the mean lactate flux across cells (coinciding with the ensemble average  $\langle u_L \rangle$  for large  $N$ , see also Supplementary Method 3), and

$$\sum_{j \neq i} A_{ij} u_L^{(j)} \simeq N \bar{u}_L \frac{R}{d} = \alpha R L \rho \bar{u}_L, \quad (16)$$

with  $d$  the mean cell-to-cell distance in a square of size  $L$ ,  $\rho = N/L^2$  the density of cells, and  $\alpha \simeq 1.918$  a numerical constant. It then follows that  $K \simeq \alpha R L \rho$  (see Supplementary Note 1 for the actual numerical values). Within this

approximation, we therefore re-write (6) as

$$u_L^{(i)} + K \bar{u}_L \leq 0 \quad (i = 1, 2, \dots, N). \quad (17)$$

One sees that, from a physical viewpoint, our choice is equivalent to assuming that the lactate flux of every cell in the population is coupled to a bulk lactate flux to which all cells contribute. This is known in physics as a ‘mean-field approximation’ (e.g., see ref. 40, Ch. 3).

A detailed examination of the mean-field model is presented in Supplementary Method 3, including the analytical solution in the limit  $N \rightarrow \infty$ . Crucially, in this approximation the constraints (6) become formally identical for all  $i$  (see (17)), which effectively reduces the study of the multi-cellular space  $\mathcal{F}_N$  to that of the single-cell space  $\mathcal{F}_1$  supplemented with the additional constraint (17). The mean-field approximation leads in turn to non-linear self-consistency equations for two emerging order parameters, one of which can be identified, in the thermodynamic limit, with the average net lactate flux  $\langle u_L \rangle$ . The equations admit an explicit analytical solution only for  $\langle u_L \rangle < -U_O/(3K)$ ; for larger  $\langle u_L \rangle$  they have to be solved numerically. The presence of background lactate can be accounted for by adding a constant to the term  $K \bar{u}_L$  in the equations (Supplementary Method 4).

The numerical solution for  $\langle u_L \rangle$  versus  $\beta_G$  at fixed  $\beta_O$  quantitatively reproduces the sampling results of the previous section (see Fig. 3a, compare with Fig. 2c). Furthermore, we found that the derivative of  $\langle u_L \rangle$  displays a discontinuity at the onset point of overflow metabolism. The values of  $\beta_O$  and  $\beta_G$  where the discontinuity occurs define a curve in the  $(\beta_O, \beta_G)$  plane that separates a phase with large lactate spillover (‘overflow phase’, above the curve) from one without (‘balanced phase’, below the curve). Such a curve is displayed in Fig. 3d. Points along the curve denote critical values of  $(\beta_G, \beta_O)$  corresponding to the transition between the two regimes. The comparison between numerical simulations and the mean-field analytical predictions shows an excellent quantitative agreement for the flux averages over the whole range of parameters, as well as for the average flux fluctuations ( $\sigma_{\langle u_L \rangle}$ ) in the unbalanced phase. However, mean-field theory underestimates fluctuations below the phase transition, see Fig. 3c. This is an expected pitfall of mean-field approximations, and more refined combinatorial<sup>42</sup> or field-theoretic<sup>40</sup> calculations would be required to overcome it.

A key difference between the two phases is the presence of negative inter-cellular flux correlations in the balanced phase that are absent in the overflow phase, where fluctuations approximately follow the law of large numbers ( $\sigma_{\langle u_L \rangle} \simeq \sigma_{u_L} / \sqrt{N}$ , as can be seen from continuous vs dashed blue lines in Fig. 3c, see also Supplementary Method 6). Our results therefore support the idea that the management of lactate levels in the medium is a genuine emergent phenomenon, achieved through a population-level coordination of lactate exchange fluxes. Likewise, coordination failures triggered by small changes in  $\beta_G$  and/or  $\beta_O$  can lead to excess accumulation of extra-cellular lactate.

### Inverse modeling experimental data

To compare our theoretical scenario with actual experimental data, we focused on recent experiments characterising the dynamical pH landscape in co-cultures of human pancreatic cancer cells (AsPC-1) and cancer-associated fibroblasts<sup>31</sup>. Advances in nanofibers technology have now made it possible to probe the cellular microenvironment in cultures at high spatial and temporal resolution<sup>43</sup>. In the dataset we considered, local pH data were collected every 10 min over a 6 h timespan, yielding 36 snapshots of the population’s adaptation (lag phase) to the culture medium. Time-resolved estimates for single-cell lactate fluxes have been previously calculated from extracellular proton levels (see ref. 31 and Supplementary Method 7). A highly heterogeneous flux profile was found, suggesting a complex underlying lactate exchange network.

We used these single-cell flux data to inform a constrained maximum-likelihood inference problem returning the values of  $\beta_G$  and  $\beta_O$  that, at each time frame, yield the best prediction of the empirical bulk lactate flux, the single-cell standard deviation, and correlations between the lactate fluxes of

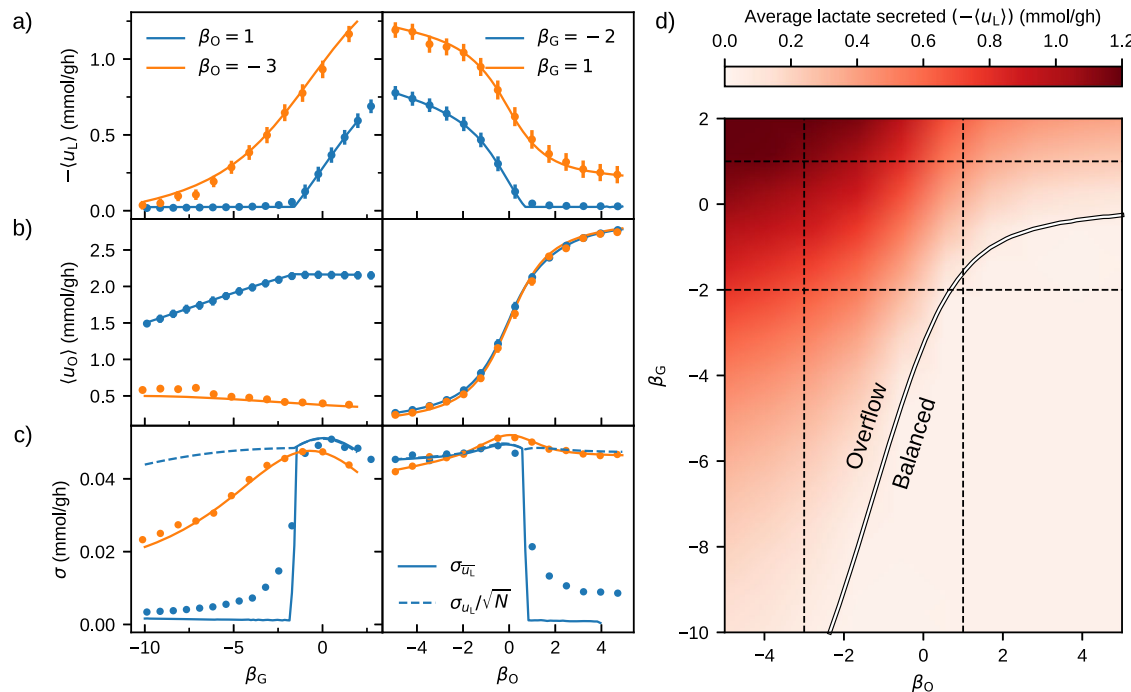


**Fig. 3 | Mean-field approximation of the CBM simulations.** Comparison between mean-field analytics (lines) and numerical simulations (points) for (a) the mean lactate flux ( $-\langle u_L \rangle$ ), (b) mean oxygen flux ( $\langle u_O \rangle$ ), and (c) standard deviation of the mean lactate flux ( $\sigma_{\bar{u}_L}$ , the dashed lines stand for the single cell standard deviation) as functions of  $\beta_G$  at fixed  $\beta_O$  (left), and of  $\beta_O$  at fixed  $\beta_G$  (right). Error bars everywhere indicate the standard error on the quantities. Simulations were performed by sampling the feasible space  $\mathcal{F}_N$  of  $N = 150$  cells spread in an area of

$500 \times 500 \mu\text{m}^2$  according to (13) via Hit-and-Run Monte Carlo Markov chains. Analytical lines were obtained by solving the mean-field model (Supplementary Method 3). **d** Mean-field phase diagram in the plane spanned by  $\beta_O$  and  $\beta_G$ . The white line is a line of phase transitions where average flux variances are discontinuous (see panel (c)), and separates the ‘overflow phase’ (above the line) from the ‘balanced phase’ (below), the two differing by the rate of lactate accumulation in the medium (background color scale).

nearest-neighbor cells, i.e.,

$$C_{\text{n.n.}} = \frac{1}{N} \sum_{i=1}^N u_L^{(i)} u_L^{(n(i))}, \quad (18)$$

where  $n(i)$  denotes the nearest neighbor of cell  $i$ . The inference pipeline is described in detail in Supplementary Method 8.  $C_{\text{n.n.}}$  plays an especially important role. In a system of non-interacting cells behaving independently,  $C_{\text{n.n.}}$  would be constrained to be positive definite (and equal to the square of the average flux, see Supplementary Method 6). Empirical values of  $C_{\text{n.n.}}$  however strongly deviate from this expectation both in absolute value and in sign (Supplementary Method 6), thereby stressing the need for an interacting model. Further, a non-interacting model made of isolated single cells is unable to fit experimental fluctuations and averages of the lactate fluxes given its strongly constrained scaling behavior (Supplementary Method 8). Global diffusion constraints like (6) indeed enable for both negative correlations and larger absolute values thereof (Supplementary Method 8). To obtain quantitative agreement, however, we found that one must account for two additional ingredients. First is the lactate accumulating in the medium over time, which, as said above, alters the form of (6) (Supplementary Method 4). The net effect of a constant background term in the mean-field model is a downward shift of the line separating the overflow from the balanced regime in the  $(\beta_O, \beta_G)$  plane (Supplementary Method 4). In experiments, the bulk lactate level was found to increase over time at a rate that decreases in time<sup>31</sup> (See also Supplementary Method 7). In such a scenario, the critical line of the mean-field model is expected to move downward in time. During most of the experiment, the empirical bulk lactate level appears to have a small impact on the population, as e.g.  $C_{\text{n.n.}}$  stays positive. In the last two hours, however, when the background lactate concentration exceeds around  $30 \mu\text{M}$ ,  $C_{\text{n.n.}}$  becomes negative (implying net exchanges between neighbors) with a small net lactate intake. The latter is at odds with empirical data, which display that lactate is on average still

excreted, albeit at reduced rates (Supplementary Method 7). We therefore solved this quantitative inconsistency by adding to the likelihood function a small phenomenological constant  $J > 0$  coupling nearest neighbors, which amounts to including a factor of the form

$$\exp \left[ -J \sum_{i=1}^N u_L^{(i)} u_L^{(n(i))} \right] \quad (19)$$

in the Boltzmann weight. While it is necessary to fully recover empirical data, this term only causes a small perturbation when accounted for in the mean-field model (Supplementary Method 6).

To summarize, the inference protocol is based on three fitting parameters, namely  $\beta_O$  and  $\beta_G$  (which take a different value for each time frame), plus the coupling constant  $J > 0$  (which instead is the same for all frames). The complete likelihood function is reported in Supplementary Method 10, along with the details of the inference pipeline.

Results are reported in Fig. 4. Panels (a) and (b) display a comparison between lactate levels and fluxes from empirical data and simulations respectively (obtained by sampling the inferred model) over time, showing for simplicity a reduced set of 6 frames (every hour). Besides the qualitative frame-by-frame agreement, one can see how inferred models quantitatively capture the dynamics of the culture by comparing empirical and model-derived time trends of bulk lactate flux (Fig. 4c), single-cell variability (Fig. 4d) and nearest-neighbor correlations (Fig. 4e). Note that, in order to appraise the predictive capabilities of the model, data were divided into a training set and a test set (ratio 9 to 1). A very good agreement is found, for both the training and test sets (reduced  $\chi^2_{\text{training}} \simeq \chi^2_{\text{test}} \simeq 0.8$ ).

We next mapped the values of  $(\beta_O, \beta_G)$  that provide the best fits over time onto the phase diagram obtained from the mean-field model (Fig. 4f). Following a transient, the points display a clear time-ordering (i.e. a rather well defined trajectory in the  $(\beta_O, \beta_G)$  plane), which suggests a strong

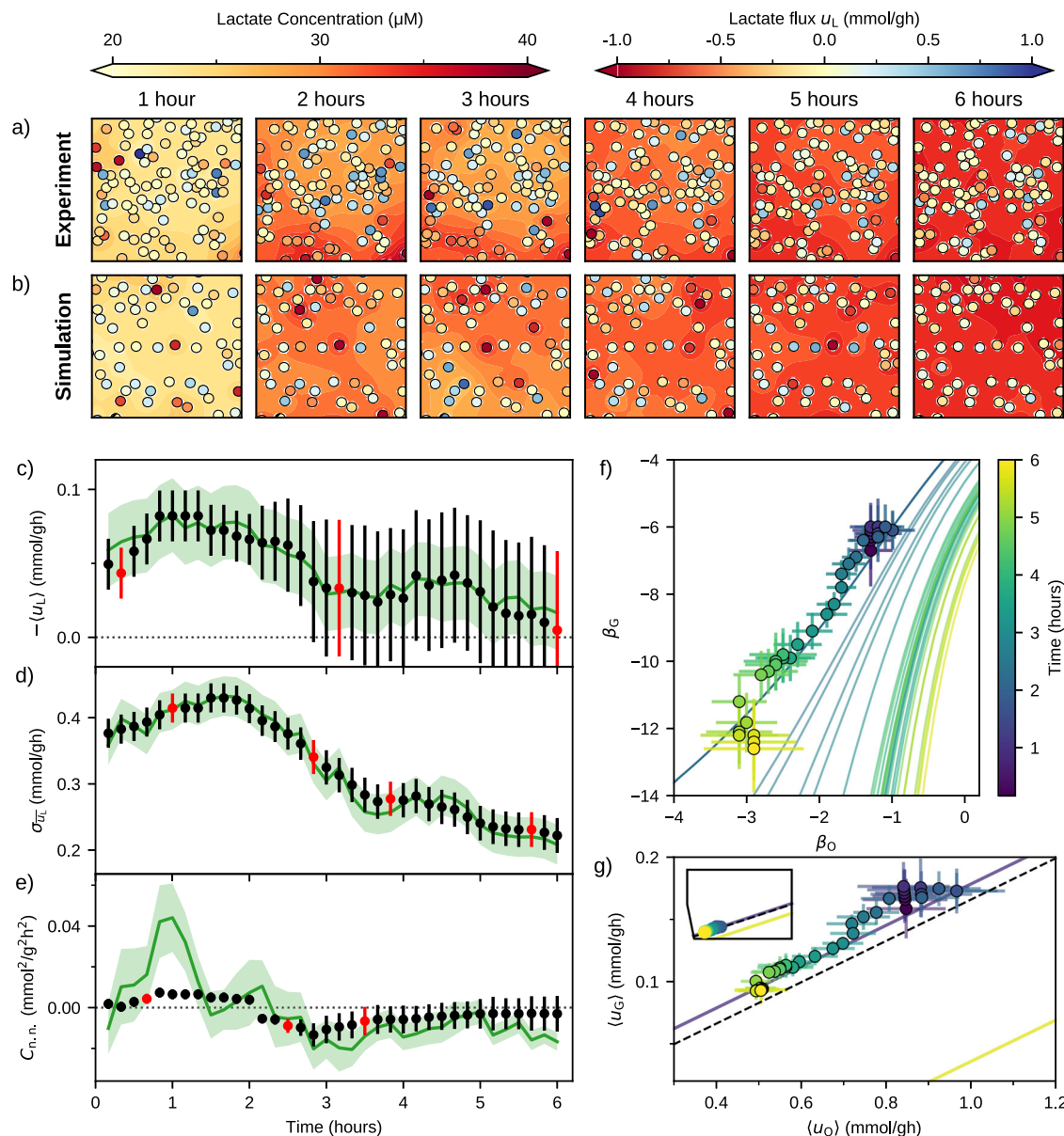


**Fig. 4 | Comparison between theoretical results and empirical data.** Snapshots of lactate gradient and single-cell fluxes from (a) experimental frames of ref. 31 (at intervals of 1 hour) and (b) from CBM simulations performed by sampling (13) with parameters  $\beta_G$  and  $\beta_O$  that, at each time step, provide the maximum likelihood reconstruction of the empirical average lactate flux. See Supplementary Method 8 for details. Comparison between empirical (line: mean value, shaded region: standard error from jackknife resampling) and theoretical (error bars; black: fit, red: prediction) flux values as a function of time for (c) mean lactate flux, (d) standard deviation of single cell lactate flux and (e) nearest-neighbor correlations. The errors

on the inferred quantities were calculated from the errors on the inferred values of  $\beta_G$  and  $\beta_O$ . f Mean-field phase diagram with the critical lines and the inferred values of  $\beta_O$  and  $\beta_G$  (markers with error bars) colored according to the time stamp for the 36 frames of the experimental dataset. For details on how the errors were estimated, see Supplementary Method 8. g Same as (f), but in the plane  $(\langle u_O \rangle, \langle u_G \rangle)$ . Only the first and last critical lines are shown. The dashed black line corresponds to  $\langle u_L \rangle = 0$ . (Note that the latter line does not appear in (f)). Inset: zoomed out view in the single-cell flux space  $\mathcal{F}_1$  of Fig. 1b.

population-level regulation of both  $\beta_G$  and  $\beta_O$  toward negative values: over time, the population appears to reduce its overall metabolic rate. A different representation of the same result is given in Fig. 4g, where the average net glucose and oxygen fluxes ( $\langle u_G \rangle$  and  $\langle u_O \rangle$ , respectively) are used as control parameters instead of  $\beta_G$  and  $\beta_O$ . In short, as time progresses and lactate accumulates in the medium, the population exhibits greater metabolic coordination (reflected in negative correlations), so that the spillover reduces in time in spite of the presence of cells that sustain large lactate export fluxes. In other terms, CO at the level of single cells does not necessarily imply environmental spillover of lactate. Furthermore, since both the inferred  $\beta_G$  and  $\beta_O$  tend to decrease in time as adaptation to the medium progresses, this population appears to move in the single-cell space

$\mathcal{F}_1$  close to the  $u_L = 0$  line and (roughly) toward the state of optimal ATP yield (see Fig. 4g versus Fig. 1b). However, because the threshold for the balanced phase shifts over time due to accumulating lactate, the population, while reducing lactate spillover, remains in the overflow regime throughout the dynamics.

#### Mitochondrial saturation versus local hypoxia: dynamics of oxygen usage

In light of the above results, it would be important to understand whether, in the observed scenario, lactate excretion by individual cells is triggered by saturated mitochondrial capacity (which diverts excess carbon towards fermentation) or, rather, by local hypoxic conditions (which limit the

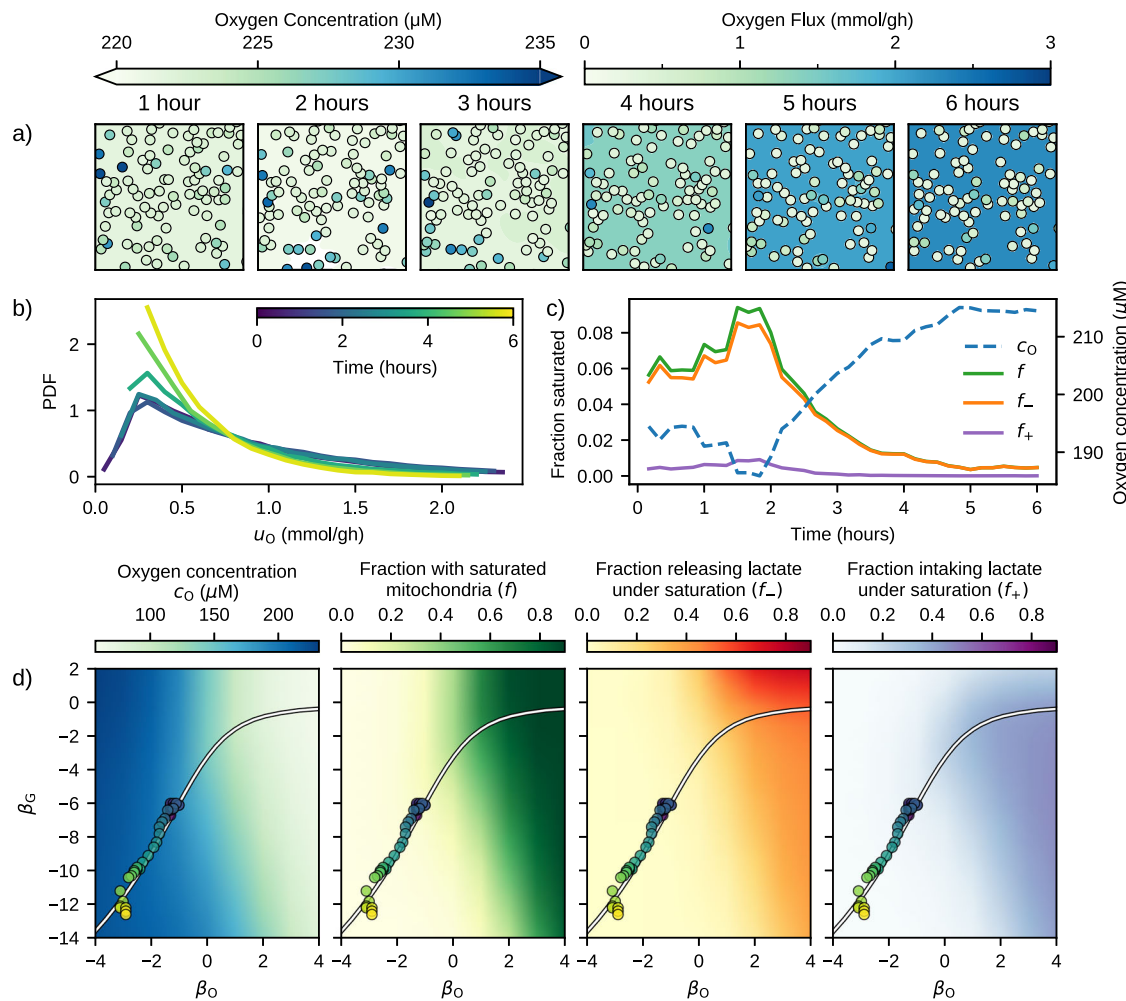


**Fig. 5 | Inferred dynamics of oxygen usage.** **a** Snapshots of oxygen levels and single-cell fluxes inferred from experimental frames (at intervals of 1 hour). Note that oxygen fluxes cannot exceed the value  $U_O = 3 \text{ mmol/g h}$  (see (4)). See Supplementary Note 1 for details. **b** Normalized histogram of inferred single-cell oxygen fluxes at different times from coarse-grained snapshots. **c** Inferred time course for bulk oxygen level ( $c_O$ ), fraction of cells with saturated oxidative capacity ( $f$ ), and

fraction of saturated cells with lactate release ( $f_-$ ) and import ( $f_+$ ). Note:  $f = f_- + f_+$ . **d** Mean-field phase diagram in the  $(\beta_O, \beta_G)$  plane plotted using the corresponding values of  $c_O, f, f_-$  and  $f_+$  as a background heat map. The critical line is in white, while values of  $\beta_O$  and  $\beta_G$  (markers) inferred from the 36 frames of the experimental dataset of<sup>31</sup> are colored according to their time stamp. For visual clarity, only the first critical line is shown.

oxidative processing of nutrients). Within the framework of our model, cell  $i$  has saturated mitochondrial capacity if its oxygen import flux  $u_O^{(i)}$  is close to the limit  $U_O = 3 \text{ mmol/g h}$  (see (4)); on the other hand, it suffers from local hypoxic conditions if it experiences a local concentration of oxygen so small that its oxygen import flux becomes diffusion-limited. In this case, a diffusion constraint for oxygen would kick in, of the form

$$u_O^{(i)} + \sum_{j \neq i} \frac{u_O^{(j)}}{|\mathbf{r}_i - \mathbf{r}_j|/R} \simeq 4\pi D_O R c_{O,\infty}, \quad (20)$$

with  $c_{O,\infty} \simeq 250 \mu\text{M}$  the background oxygen concentration (Eq. (20)) expresses that fact that the concentration of oxygen at the boundary of cell  $i$  is  $c_O^{(i)} \simeq 0$ , see Supplementary Note 2).

In absence of high-resolution data about local oxygen levels in the culture, addressing this question requires an inference framework that goes from learning distributions to learning single-cell fluxes. We can however use single-cell lactate fluxes derived from the dataset of<sup>31</sup>, along with the estimate for the average oxygen flux derived above, to obtain a prediction for single-cell oxidative fluxes via a Boltzmann sampling of the  $N$ -cell space of feasible flux configurations  $\mathcal{F}_N$ . Theoretical and computational details of the method employed are given in Supplementary Method 9. While

single-cell oxygen fluxes show large uncertainties due to the “sloppiness”<sup>44</sup> of the inferred model, we can reconstruct a plausible scenario whose key results are given in Fig. 5.

We first notice (Fig. 5a) that, due to a faster diffusion rate, oxygen profiles across the culture appear much more homogeneous than lactate profiles. In addition, single-cell fluxes display a time trend towards down-regulation and reduced heterogeneity, a pattern consistent with the time-course of  $\beta_O$  shown in Fig. 4f. This is quantified by how the normalized histogram of single-cell  $u_O$  values shifts over time (Fig. 5b). Cells sustaining an oxygen import flux closer to the saturation point ( $U_O \sim 2-3 \text{ mmol/g h}$ , see (4)) become rarer as time progresses.

A closer look at the time course (Fig. 5c) highlights two distinct regimes in the population’s dynamics. While remaining consistently below 10%, the fraction  $f$  of saturated mitochondria initially increases as cells seem to increase oxygen consumption (consistently with the transient increase of  $\beta_O$  that is visible in Fig. 4f), leading to a decrease of average environmental oxygen levels  $c_O$ . After about 2 hours,  $f$  inverts the trend and begins to decrease while  $c_O$  concomitantly increases, signaling that cells have stabilized their metabolism at reduced levels of lactate export, import and exchange (Fig. 4a-d). Note that mitochondrial saturation can occur both under excess glucose intake, leading to the release of lactate in the medium, and under intake of lactate from the medium. We denote by  $f_-$  (resp.  $f_+$ ) the

fraction of cells in the former (resp. latter) condition. Figure 5c shows that, while (perhaps surprisingly) saturation with lactate import is more common, both  $f_+$  and  $f_-$  follow the same time trend as  $f$ .

Overall, these results, along with evidence that oxygen concentration consistently stays above typical hypoxia levels ( $2\text{--}3 \text{ mg/L of O}_2 \simeq 60 \mu\text{mol/L}$ <sup>45</sup>), imply that the inferred single-cell oxygen fluxes stay well above the diffusion limit in our experimental conditions (see also Supplementary Method 5). This suggests that the observed dynamics is more likely coupled to the collective behavior of the population and the emergent exchange network than to a depletion of local environmental oxygen.

To further support this picture, it is useful to revisit the phase structure of Fig. 4f against the background of the quantities used to analyze oxygen dynamics, reported in detail in Fig. 5d. While macroscopic features appear to be strongly tied to the value of  $\beta_O$ , one notices that the region where acidification is most severe ( $\beta_G > 0, \beta_O < 0$ ) is not generically associated to hypoxic conditions or mitochondrial saturation and, again, both conditions characterize the region where acidification is mild ( $\beta_G < 0, \beta_O > 0$ ). This shows that single-cell and population-level features are separated, the latter being essentially driven by inter-cellular interactions.

## Discussion

The broad biological question we faced here asks whether the metabolic phenotype of a multi-cellular system emerges from the interactions among its individual components or is rather the result of a multitude of independent cell-autonomous behaviors. The results we present support the idea that metabolic interactions between cells play a central role in shaping their shared environment, thus influencing the overall fitness of the population. More precisely, cells appear to collectively regulate the levels of medium-acidifying compounds through time-dependent coordination of their exchanges with the surroundings. This process is ultimately sustained by the establishment of cell-to-cell interactions facilitated by the transport of overflow products. In the presence of coordination, environmental spillover is limited despite the presence of cells exporting these compounds at high rates. Conversely, the accumulation of compounds in the medium can be seen as a failure to coordinate.

Our findings furthermore provide robust evidence that the large-scale metabolic organization of cell populations exhibits hallmarks of phase transitions, and may therefore be understood, and possibly controlled, through the application of concepts derived from statistical physics. Indeed, when viewed through the lens of collective phenomena, the crossover from a balanced to an unbalanced state with overflow metabolism bears significant similarities to the standard disorder-to-order transitions that occur, for example, in magnetic systems. These models have shown that highly non-trivial macroscopic properties can arise from the interaction patterns of large assemblies of simple, identical variables<sup>30</sup>. In recent years, many of the methods and insights developed for the study of these systems have been ported to other disciplines, including ecology<sup>46–48</sup>. In view of its focus on inter-cellular couplings and their consequences, our work is indeed close to ecological settings, albeit perhaps on the more basic ground of cellular metabolic dynamics.

Finally, our results confirm that heterogeneous cell populations can be described effectively by maximum-entropy distributions like (9)<sup>38,39,49–53</sup>, suggesting that, at least in some conditions, the constrained maximisation of population-level variability might be a reasonable objective for multi-cellular systems.

On the more biological side, the inverse-modeling scheme we developed indicates quantitative ways to appraise the adaptive metabolic response of populations of cells to their environment, with single-cell resolution. As a plus, our protocol requires inferring only a small number of parameters and constraints in order to effectively describe the metabolism of large, spatially organized populations over time. This stands in contrast to the complex task of inverse modeling spiking data using e.g. Ising neural networks, which typically demands the inference of one parameter per synaptic connection<sup>54</sup>. Upon analyzing experimental data from real tumor-stroma cell cultures during the adaptation phase, we

found that cells coordinate their metabolism and reduce their metabolic rate over time to prevent environmental deterioration caused by lactic acid overflow. Further analysis indicates that individual cells operate far from mitochondrial saturation and well below the oxygen diffusion limit (i.e., away from local hypoxia). Overall, this picture strongly suggests that the primary driver of the observed population-level dynamics is not to be found in metabolic constraints but, rather, in a failure of cellular coordination. We showed that a version of the model made of isolated single cells (the usual assumption of flux balance analysis models<sup>35</sup>) is unable by construction to retrieve observed negative cell-cell correlations and the fluctuations scaling of metabolic fluxes (Supplementary Method 8). Unfortunately, such a scenario could only be validated using a single dataset, and should ideally be contrasted with single-cell flux data taken in different experimental conditions (e.g., different cell populations, density, geometry and medium composition). Although recent advancements in high resolution mass-spectrometry hold promise<sup>55,56</sup>, they are currently expensive and invasive. On the other hand, the very recent development of micro-environmental sensing protocols<sup>57–60</sup>, coupled with ad hoc inverse modeling schemes, has the potential to lead to fully time-resolved single-cell metabolic flux analysis.

Besides the highly simplifying assumptions on which it relies, the major limitation of our theoretical work lies, we believe, in its static (quasi-equilibrium) character. A constant background lactate level allows for the analytical tractability that, in turn, unravels the connection between overflow phenomena and phase transitions. Empirical data are however not stationary. In our case study, this aspect appears to become especially important only in the final part of the adaptation dynamics. To make our theoretical framework applicable to more general datasets, it will however be important to explicitly consider the coupled dynamics of the state of environment and the behavior of cells. This could generalize models of population metabolism that rely on the assumption of single cell optimality (like COMETS<sup>61</sup>). Such an implementation could benefit from recent generalization of the maximum-entropy scheme in out-of-equilibrium settings known as maximum-caliber<sup>62</sup>.

In addition to fundamental aspects, our work offers insights in the context of tumor metabolism. In higher organisms, where metabolic behavior is specialized and compartmentalized according to cell type, the exchange of metabolites such as lactate occurs across multiple scales: organs, tissue and single cells<sup>63</sup>. This division of labor through metabolic specialization and exchange provides significant benefit to healthy tissues. However, it also renders these systems vulnerable to exploitation by malignant cells, which undergo metabolic rewiring during carcinogenesis<sup>64</sup>. As first observed by Warburg in the 1920s<sup>65</sup>, tumours exhibit a notable tendency to consume excessive amounts of glucose while producing lactate, even in the presence of oxygen. However, despite extensive research efforts, a comprehensive understanding of the Warburg effect in cancer has remained elusive to date<sup>66</sup>. The approach presented herein supports the idea that the Warburg effect may reflect an emergent feature of a large population of interacting cells characterized by a highly heterogeneous pattern of lactate exchange among individual cells. This in turn would place considerable weight on the ecological dynamics of tumor development, particularly in its early stages. Such a scenario would be fully consistent with recent experimental findings<sup>67</sup>.

## Methods

### Model and simulation parameters

The model parameters were chosen to closely match the experimental settings<sup>31</sup>, with approximately 40,000 cells of radius  $10 \mu\text{m}$  and dry weight  $1 \text{ ng}$  randomly distributed in an area of  $1 \text{ cm}^2$ , with background glucose ( $c_G$ ) and oxygen ( $c_O$ ) concentrations  $25 \text{ mM}$  and  $0.25 \text{ mM}$  respectively. The simulations were performed in a window of  $500 \times 500 \mu\text{m}^2$ , consisting of about 150 cells. The maximum glucose import  $U_G$  and maximum oxygen import  $U_O$  were chosen to be  $1 \text{ mmol/g h}$  and  $3 \text{ mmol/g h}$  respectively. The ATP maintenance demand  $L_M$  was fixed at  $1 \text{ mmol/g h}$ . All parameters for the model and simulations obtained from literature, including the diffusion

coefficients used for the relevant metabolites, are provided in Supplementary Table 1, along with other relevant derived quantities.

### The sampling algorithm

The space of feasible multi-cellular metabolic flux configurations  $\mathcal{F}_N$  was sampled according to the specified probability distribution (13) using a hit-and-run Markov chain algorithm. The steps are provided in detail in Supplementary Method 2. The code to perform the sampling is made available online<sup>68</sup>.

### Mean-field approximation

The detailed derivation of the explicit partition function in terms of the parameters is provided in Supplementary Method 3. See also Supplementary Method 4 for details on how the mean-field equations are modified when a background lactate term is introduced. The code to calculate various quantities under the mean-field approximation is made available online<sup>68</sup>.

### Inverse modeling experimental data

For inference of the model parameters that yield the best prediction of time-resolved experimental lactate flux data<sup>31,69</sup>, predictions from the model were fitted to key statistical features of the observed flux distribution: the average lactate flux, its standard deviation (fluctuations), and nearest-neighbor correlations. The model parameters  $\beta_G$  and  $\beta_O$  were allowed to vary for each experimental time point, and the phenomenological nearest-neighbor coupling constant was kept constant. The inference procedure involved maximizing the likelihood of experimental data and sampling parameters according to the posterior probability distribution using a Metropolis Monte-Carlo algorithm, and is described in detail in Supplementary Method 8, along with the various attempts that were made including and excluding different terms in the likelihood function before the final form was used.

### Reporting summary

Further information on research design is available in the Nature Portfolio Reporting Summary linked to this article.

### Data availability

The experimental data analyzed in this work were published previously<sup>31</sup> and are available online<sup>69</sup>.

### Code availability

The code to perform simulations, mean field calculations and inference is available online<sup>68</sup>.

Received: 18 July 2024; Accepted: 8 May 2025;

Published online: 19 May 2025

### References

1. Pfeiffer, T., Schuster, S. & Bonhoeffer, S. Cooperation and Competition in the Evolution of ATP-Producing Pathways. *Science* **292**, 504–507 (2001).
2. Vaupel, P. Metabolic microenvironment of tumor cells: a key factor in malignant progression. *Exp. Oncol.* **32**, 125–7 (2010).
3. Waltermann, C. & Klipp, E. Information theory based approaches to cellular signaling. *Biochim. et. Biophys. Acta (BBA) - Gen. Subj.* **1810**, 924–932 (2011).
4. Caulin, A. F. & Maley, C. C. Peto's Paradox: Evolution's prescription for cancer prevention. *Trends Ecol. Evol.* **26**, 175–182 (2011).
5. De Groot, D. H. et al. The common message of constraint-based optimization approaches: overflow metabolism is caused by two growth-limiting constraints. *Cell. Mol. Life Sci.* **77**, 441–453 (2020).
6. Damiani, C., Serra, R., Villani, M., Kauffman, S. & Colacci, A. Cell-cell interaction and diversity of emergent behaviours. *IET Syst. Biol.* **5**, 137–144 (2011).
7. Wolfe, A. J. The acetate switch. *Microbiol. Mol. Biol. Rev.* **69**, 12–50 (2005).
8. Vazquez, A. *Overflow metabolism: from yeast to marathon runners* (Academic Press, Cambridge, MA (USA), 2017).
9. Wang, Y. et al. Saturation of the mitochondrial nadh shuttles drives aerobic glycolysis in proliferating cells. *Mol. cell* **82**, 3270–3283 (2022).
10. Vazquez, A. et al. Impact of the solvent capacity constraint on *E. coli* metabolism. *BMC Syst. Biol.* **2**, 7 (2008).
11. Shlomi, T., Benyamin, T., Gottlieb, E., Sharan, R. & Ruppin, E. Genome-Scale Metabolic Modeling Elucidates the Role of Proliferative Adaptation in Causing the Warburg Effect. *PLoS Computational Biol.* **7**, e1002018 (2011).
12. Basan, M. et al. Overflow metabolism in *Escherichia coli* results from efficient proteome allocation. *Nature* **528**, 99–104 (2015).
13. Szenk, M., Dill, K. A. & de Graff, A. M. Why do fast-growing bacteria enter overflow metabolism? testing the membrane real estate hypothesis. *Cell Syst.* **5**, 95–104 (2017).
14. Mori, M., Marinari, E. & De Martino, A. A yield-cost tradeoff governs *Escherichia coli*'s decision between fermentation and respiration in carbon-limited growth. *NPJ Syst. Biol. Appl.* **5**, 16 (2019).
15. Chen, Y. & Nielsen, J. Energy metabolism controls phenotypes by protein efficiency and allocation. *Proc. Natl Acad. Sci.* **116**, 17592–17597 (2019).
16. Vander Heiden, M. G., Cantley, L. C. & Thompson, C. B. Understanding the warburg effect: the metabolic requirements of cell proliferation. *Science* **324**, 1029–1033 (2009).
17. Hirschhaeuser, F., Sattler, U. G. A. & Mueller-Klieser, W. Lactate: A metabolic key player in cancer. *Cancer Res.* **71**, 6921–6925 (2011).
18. Vazquez, A. et al. Cancer metabolism at a glance. *J. Cell Sci.* **129**, 3367–3373 (2016).
19. Sullivan, L. B., Gui, D. Y. & Heiden, M. G. V. Altered metabolite levels in cancer: implications for tumour biology and cancer therapy. *Nat. Rev. Cancer.* <http://www.nature.com/doifinder/10.1038/nrc.2016.85> (2016).
20. Kukuruya, M. A. & Titov, D. V. The warburg effect is the result of faster atp production by glycolysis than respiration. *bioRxiv* 2022–12 (2022).
21. Shen, Y. et al. Mitochondrial ATP generation is more proteome efficient than glycolysis. *Nat. Chem. Biol.* **20**, 1123–1132 (2024).
22. de la Cruz-López, K. G., Castro-Muñoz, L. J., Reyes-Hernández, D. O., García-Carrancá, A. & Manzo-Merino, J. Lactate in the regulation of tumor microenvironment and therapeutic approaches. *Front. Oncol.* **9**, 1143 (2019).
23. Mason, S. Lactate shuttles in neuroenergetics-homeostasis, allostasis and beyond. *Front. Neurosci.* **11**, 43 (2017).
24. Millard, P., Uttenweiler-Joseph, S. & Enjalbert, B. From toxic waste to beneficial nutrient: acetate boosts *Escherichia coli* growth at low glycolytic flux. *bioRxiv* 2022–09 (2022).
25. Liberti, M. V. & Locasale, J. W. The warburg effect: how does it benefit cancer cells? *Trends Biochem. Sci.* **41**, 211–218 (2016).
26. Fernandez-de Cossio-Diaz, J., De Martino, A. & Mulet, R. Microenvironmental cooperation promotes early spread and bistability of a warburg-like phenotype. *Sci. Rep.* **7**, 3103 (2017).
27. Wang, X., Liu, H., Ni, Y., Shen, P. & Han, X. Lactate shuttle: from substance exchange to regulatory mechanism. *Human Cell* **35**, 1–14 (2022).
28. Hershey, B. J. et al. Clonal cooperation through soluble metabolite exchange facilitates metastatic outgrowth by modulating allel effect. *Sci. Adv.* **9**, eadhd4184 (2023).
29. Bordbar, A., Monk, J. M., King, Z. A. & Palsson, B. O. Constraint-based models predict metabolic and associated cellular functions. *Nat. Rev. Genet.* **15**, 107–120 (2014).
30. Nishimori, H. & Ortiz, G. *Elements of phase transitions and critical phenomena* (Oxford University Press, Oxford (UK), 2011).
31. Onesto, V. et al. Probing single-cell fermentation fluxes and exchange networks via ph-sensing hybrid nanofibers. *ACS nano* **17**, 3313–3323 (2022).

32. Milo, R. & Phillips, R. *Cell biology by the numbers*. 1st edn, <https://doi.org/10.1201/9780429258770> (Garland Science, New York (NY, USA), 2015).

33. Park, J. O. et al. Metabolite concentrations, fluxes and free energies imply efficient enzyme usage. *Nat. Chem. Biol.* **12**, 482–489 (2016).

34. De Martino, D. Genome-scale estimate of the metabolic turnover of *e. coli* from the energy balance analysis. *Phys. Biol.* **13**, 016003 (2016).

35. Orth, J. D., Thiele, I. & Palsson, B. Ø. What is flux balance analysis? *Nat. Biotechnol.* **28**, 245–248 (2010).

36. Capuani, F., De Martino, D., Marinari, E. & De Martino, A. Quantitative constraint-based computational model of tumor-to-stroma coupling via lactate shuttle. *Sci. Rep.* **5**, 11880 (2015).

37. De Martino, A. & De Martino, D. An introduction to the maximum entropy approach and its application to inference problems in biology. *Heliyon* **4** (2018).

38. De Martino, D., Capuani, F. & De Martino, A. Growth against entropy in bacterial metabolism: the phenotypic trade-off behind empirical growth rate distributions in *e. coli*. *Phys. Biol.* **13**, 036005 (2016).

39. De Martino, D., Mc Andersson, A., Bergmiller, T., Guet, C. C. & Tkačik, G. Statistical mechanics for metabolic networks during steady state growth. *Nat. Commun.* **9**, 2988 (2018).

40. Parisi, G. *Statistical Field Theory (Advanced Book Classics)* (Perseus Pr, New York (NY, USA), 1998).

41. Niebel, B., Leupold, S. & Heinemann, M. An upper limit on gibbs energy dissipation governs cellular metabolism. *Nat. Metab.* **1**, 125–132 (2019).

42. Baxter, R. J. *Exactly solved models in statistical mechanics* (Dover, New York (NY, USA), 2016).

43. Moldero, I. L. et al. Probing the ph microenvironment of mesenchymal stromal cell cultures on additive-manufactured scaffolds. *Small* **16**, 2002258 (2020).

44. Gutenkunst, R. N. et al. Universally sloppy parameter sensitivities in systems biology models. *PLoS computational Biol.* **3**, e189 (2007).

45. Herman, I. P. *Physics of the human body* (Springer, Berlin (Germany), 2016).

46. Advani, M., Bunin, G. & Mehta, P. Statistical physics of community ecology: a cavity solution to macarthur's consumer resource model. *J. Stat. Mech.: Theory Exp.* **2018**, 033406 (2018).

47. Altieri, A. & Franz, S. Constraint satisfaction mechanisms for marginal stability and criticality in large ecosystems. *Phys. Rev. E* **99**, 010401 (2019).

48. Batista-Tomás, A., De Martino, A. & Mulet, R. Path-integral solution of macarthur's resource-competition model for large ecosystems with random species-resources couplings. *Chaos: An Interdisciplinary Journal of Nonlinear Science* **31** (2021).

49. Fernandez-de-Cossio-Diaz, J., Leon, K. & Mulet, R. Characterizing steady states of genome-scale metabolic networks in continuous cell cultures. *PLoS Computational Biol.* **13**, 1–22 (2017).

50. Fernandez-de-Cossio-Diaz, J. & Mulet, R. Maximum entropy and population heterogeneity in continuous cell cultures. *PLoS Computational Biol.* **15**, e1006823 (2019).

51. Fernandez-de-Cossio-Diaz, J. & Mulet, R. Statistical mechanics of interacting metabolic networks. *Phys. Rev. E* **123**, 52–69 (2020).

52. Tourigny, D. S. Dynamic metabolic resource allocation based on the maximum entropy principle. *J. Math. Biol.* **80**, 2395–2430 (2020).

53. Rivas-Astroza, M. & Conejeros, R. Metabolic flux configuration determination using information entropy. *Plos one* **15**, e0243067 (2020).

54. Schneidman, E., Berry, M. J., Segev, R. & Bialek, W. Weak pairwise correlations imply strongly correlated network states in a neural population. *Nature* **440**, 1007–1012 (2006).

55. Wang, L. et al. Spatially resolved isotope tracing reveals tissue metabolic activity. *Nat. methods* **19**, 223–230 (2022).

56. Rappez, L. et al. Spacem reveals metabolic states of single cells. *Nat. methods* **18**, 799–805 (2021).

57. Rizzo, R. et al. ph-sensing hybrid hydrogels for non-invasive metabolism monitoring in tumor spheroids. *Mater. Today Bio* **20**, 100655 (2023).

58. Grasso, G. et al. Fluorescent nano-and microparticles for sensing cellular microenvironment: past, present and future applications. *Nanoscale advances* (2023).

59. Feng, Q. et al. Severely polarized extracellular acidity around tumour cells. *Nature Biomedical Engineering* 1–13 (2024).

60. Grasso, G. et al. Highly sensitive ratiometric fluorescent fiber matrices for oxygen sensing with micrometer spatial resolution. *Bio-Design and Manufacturing* 1–15 (2024).

61. Dukovski, I. et al. A metabolic modeling platform for the computation of microbial ecosystems in time and space (comets). *Nat. Protoc.* **16**, 5030–5082 (2021).

62. Ghosh, K., Dixit, P. D., Agozzino, L. & Dill, K. A. The maximum caliber variational principle for nonequilibria. *Annu. Rev. Phys. Chem.* **71**, 213–238 (2020).

63. Brooks, G. A. Cell–cell and intracellular lactate shuttles. *J. Physiol.* **587**, 5591–5600 (2009).

64. Pavlova, N. N., Zhu, J. & Thompson, C. B. The hallmarks of cancer metabolism: Still emerging. *Cell metabolism* (2022).

65. Warburg, O. The Metabolism of Carcinoma Cells. *J. Cancer Res.* **9**, 148–163 (1925).

66. DeBerardinis, R. J. & Chandel, N. S. We need to talk about the warburg effect. *Nat. Metab.* **2**, 127–129 (2020).

67. Hensley, C. T. et al. Metabolic heterogeneity in human lung tumors. *Cell* **164**, 681–694 (2016).

68. Narayanan, K. Multicellular metabolic networks: Initial release. <https://zenodo.org/doi/10.5281/zenodo.12771735> (2024).

69. Martino, D. D. Probing single-cell fermentation fluxes. <https://zenodo.org/doi/10.5281/zenodo.12772220> (2024).

## Acknowledgements

K.N. and D.D.M. thank the FBB (Fundación Biofísica Bizkaia) for support. D.D.M. acknowledges financial support from the grants PIBA\_2024\_1\_0016 (Basque Government) and Project PID2023-146408NB-I00 funded by MICIU/AEI/10.13039/501100011033 and by FEDER, UE. J.A.P.M., R.M., and A.D.M. acknowledge financial support from the European REA, Marie Skłodowska-Curie Actions, grant agreement no. 101131463 (SIMBAD). DST thanks Biofísika Institute for hosting him while part of this work was carried out. L.L.D.M. thanks the Associazione Italiana per la Ricerca contro il Cancro (AIRC) (MFAG-2019, n. 22902), the PRIN 2022 (2022CRFNCP) funded by the Italian Ministry of Research (MUR) European Union - Next Generation EU and the Italian Ministry of Research, under the complementary actions to the NRRP 'Fit4MedRob - Fit for Medical Robotics' Grant (#PNC0000007). A.F.F. acknowledges support from the Predoctoral Training Program for Non-Doctoral Research Personnel of the Basque Government's Department of Education.

## Author contributions

Conceptualization: D.D.M., D.T., A.D.M., R.M., and L.D.M.; Modeling: K.N., J.A.P.M., A.F., D.D.M., D.T., A.D.M., and R.M.; Simulations: K.N., J.A.P.M. and D.D.M.; Analytical calculations: K.N., D.D.M., D.T. and A.D.M.; Data Analysis and Inference: K.N., J.A.P.M., A.F., V.O. and D.D.M.; Experiments: V.O., S.F. and L.D.M.; Funding: D.D.M., D.T., A.D.M., R.M., and L.D.M.

## Competing interests

The authors declare no competing interests.

## Additional information

**Supplementary information** The online version contains supplementary material available at <https://doi.org/10.1038/s42005-025-02133-x>.

**Correspondence** and requests for materials should be addressed to Andrea De Martino, David S. Tourigny or Daniele De Martino.

**Peer review information** *Communications Physics* thanks the anonymous reviewers for their contribution to the peer review of this work. A peer review file is available.

**Reprints and permissions information** is available at <http://www.nature.com/reprints>

**Publisher's note** Springer Nature remains neutral with regard to jurisdictional claims in published maps and institutional affiliations.

**Open Access** This article is licensed under a Creative Commons Attribution-NonCommercial-NoDerivatives 4.0 International License, which permits any non-commercial use, sharing, distribution and reproduction in any medium or format, as long as you give appropriate credit to the original author(s) and the source, provide a link to the Creative Commons licence, and indicate if you modified the licensed material. You do not have permission under this licence to share adapted material derived from this article or parts of it. The images or other third party material in this article are included in the article's Creative Commons licence, unless indicated otherwise in a credit line to the material. If material is not included in the article's Creative Commons licence and your intended use is not permitted by statutory regulation or exceeds the permitted use, you will need to obtain permission directly from the copyright holder. To view a copy of this licence, visit <http://creativecommons.org/licenses/by-nc-nd/4.0/>.

© The Author(s) 2025